MIT Libraries | DSpace@MIT

MIT Open Access Articles

Full-waveform based microseismic source mechanism studies in the Barnett Shale: Linking microseismicity to reservoir geomechanics

Massachusetts Institute of Technology

Full-waveform based microseismic source mechanism studies in the Barnett Shale: Linking microseismicity to reservoir geomechanics

Fuxian Song[1], Norm R. Warpinski[2], and M. Nafi Toksöz[3]

ABSTRACT

Seismic moment tensors (MTs) of microearthquakes contain important information on the reservoir and fracturing mechanisms. Difficulties arise when attempting to retrieve complete MT with conventional amplitude inversion methods if only one well is available. With the full-waveform approach, near-field information and nondirect waves (i.e., refracted/reflected waves) help stabilize the inversion and retrieve complete MT from the single-well data set. However, for events which are at far field from the monitoring well, a multiple-well data set is required. In this study, we perform the inversion with a dual-array data set from a hydrofracture stimulation in the Barnett Shale. Determining source mechanisms from the inverted MTs requires the use of a source model, which in this case is the tensile earthquake model. The source information derived includes the fault plane solution, slip direction, V_P/V_S ratio in the focal area and seismic moment. The primary challenge of extracting source parameters from MT is to distinguish the fracture plane from auxiliary plane. We analyze the microseismicity using geomechanical analysis to determine the fracture plane. Furthermore, we investigate the significance of non-DC components by F-test. We also study the influence of velocity model errors, event mislocations, and data noise using synthetic data. The results of source mechanism analysis are presented for the events with good signal-to-noise ratios and low condition numbers. Some events have fracture planes with similar orientations to natural fractures delineated by core analysis, suggesting reactivation of natural fractures. Other events occur as predominantly tensile events along the unperturbed maximum horizontal principal stress direction, indicating an opening mode failure on hydraulic fractures. Microseismic source mechanisms not only reveal important information about fracturing mechanisms, but also allow fracture characterization away from the wellbore, providing critical constraints for understanding fractured reservoirs.

INTRODUCTION

Microseismic mapping has proven valuable for monitoring stimulations in unconventional reservoirs such as gas shales (Fisher et al., 2004; Shemeta et al., 2007; Maxwell et al., 2010; Birkelo et al., 2012). Beside location, microseismic waveforms contain important information about the source mechanisms and stress state (Baig and Urbancic, 2010). The complete moment tensor (MT) of the general source mechanism consists of six independent components (Aki and Richards, 2002). Previous studies have demonstrated that conventional methods using only far-field P- and S-amplitudes from one vertical well cannot retrieve the off-plane MT component, and therefore we have to make additional assumptions, such as assuming a deviatoric source (Vavryčuk, 2007).

However, recent studies have shown the existence of non-double-couple (non-DC) mechanisms for some hydrofracture events (Šílený et al., 2009; Warpinski and Du, 2010). Knowledge of the complete MT, especially the non-DC components, is essential to understand the fracturing process especially the failure mechanisms (Šílený et al., 2009). Moreover, Vavryčuk (2007) has shown that, for shear faulting on nonplanar faults, or for tensile faulting, the deviatoric source assumption is no longer valid and neglecting it can severely distort the retrieved MT and bias the fault plane solution (FPS: strike, dip, and rake angles). Therefore, the complete MT inversion is crucial not

only to the retrieval of the non-DC components but also to the correct estimation of the fracture plane orientation.

To overcome the difficulty associated with single-well complete MT inversion, Song and Toksöz (2011) propose a full-waveform approach to invert for the complete moment tensor. They have demonstrated that the complete MT can be retrieved from a single-well data set by inverting the full waveforms, if the events are close to the monitoring well. It has been shown that the near-field information and nondirect waves (i.e., reflected/refracted waves) propagated through a layered medium contribute to the decrease in the condition number of the sensitivity matrix. However, when the events are in the far-field range, at least two monitoring wells are needed for complete MT inversion. Therefore, in this paper, we invert for the complete MT to determine the microseismic source mechanisms in the Barnett Shale by using dual array data.

Determining the source mechanism from the MT requires the use of a source model. As pointed out by Vavryčuk (2011), one of the models describing the earthquake source more adequately and predicting significant non-DC components is the general dislocation model or, equivalently, the model of tensile earthquakes (Vavryčuk, 2001). This model allows the slip vector defining the displacement discontinuity on the fracture to deviate from the fracture plane. Faulting can thus accommodate shear and tensile failures. Consequently, the fracture can possibly be opened or closed during the rupture process. Tensile earthquakes have been reported in hydraulic fracturing and fluid injection experiments (Zoback, 2007; Šílený et al., 2009; Baig and Urbancic, 2010; Warpinski and Du, 2010; Song and Toksöz, 2011; Fischer and Guest, 2011). Moreover, field and experimental observations reveal that simple, planar hydraulic fractures, as commonly interpreted in many reservoir applications, are relatively rare (Busetti et al., 2012). The location analysis of microseismic events during the hydrofracture stimulation in the Barnett Shale, Fort Worth Basin, Texas, reveals complex location patterns that depend on the local stress state and proximity to folds, faults, and karst structures (Warpinski et al., 2005; Roth and Thompson, 2009). Therefore, in this study, we adopt the tensile

earthquake model to determine the microseismic source mechanisms from the inverted MT. The extracted source parameters include the FPS, the slip direction, the V_P/V_S ratio in the focal area, and the seismic moment. The determined source mechanisms are aimed to help better understand the formation of the observed complex location patterns and eventually the fracturing process in the Barnett Shale.

We select a set of events with good signal-to-noise ratios (S/Ns) and low condition numbers out of a dual-array microseismic data set from a hydraulic fracture stimulation of the Barnett Shale at Fort Worth Basin, Texas, USA. We use the discrete wavenumber integration method to calculate elastic wavefields in the layered medium (Bouchon, 2003). By matching the waveforms across the two geophone arrays, we invert for the MT of each selected event. To derive the source parameters from the MT, the fracture plane has to be separated from the auxiliary plane. To address this problem and better understand how the microseismicity is related to the fracturing process, we study the hydraulic fracture geomechanics in the Barnett Shale. Based on the observations from geomechanical analysis, we describe an approach to determine the source parameters from the inverted MT. To quantify the uncertainty of extracted source parameters, we conduct a Monte-Carlo test on synthetic data to study the influence of velocity model errors, source mislocations, and additive data noise. Furthermore, we also investigate the significance of the occurrence of non-DC components by F-test. We show that most of the events have significant non-DC components, manifested in the appearance of an off-fracture-plane slip vector. Finally, we discuss the estimated microseismic source mechanisms and their implications in understanding the fracturing process and the reservoir.

METHODOLOGY

Tensile earthquake model

To describe the complexity in the earthquake source that gives rise to the occurrence of significant non-DC components, a general tensile earthquake model was first proposed by Vavryčuk (2001) and later illustrated further by Vavryčuk (2011). In this paper, we follow the convention of Vavryčuk (2011). As shown in Figure 1, the fracture plane normal **n** and the slip vector **v**, defined in the (north, east, and downward) coordinate system, are expressed for the tensile source in terms of strike ϕ, dip δ, rake λ, and slope angle α as follows

$$n_1 = -\sin \delta \sin \phi \quad n_2 = -\sin \delta \cos \phi \quad n_3 = -\cos \delta \tag{1}$$

$$
\begin{aligned}
v_1 &= (\cos \delta \sin \lambda \sin \phi + \cos \lambda \cos \phi) \cos \alpha \\
&\quad - \sin \delta \sin \phi \sin \alpha \\
v_2 &= (-\cos \delta \sin \lambda \cos \phi + \cos \lambda \sin \phi) \cos \alpha \\
&\quad + \sin \delta \cos \phi \sin \alpha \\
v_3 &= -\sin \delta \sin \lambda \cos \alpha - \cos \delta \sin \alpha.
\end{aligned}
\tag{2}
$$

Here, strike ϕ is measured clockwise from north. The dip δ is defined as the angle between the fracture plane and the horizontal.
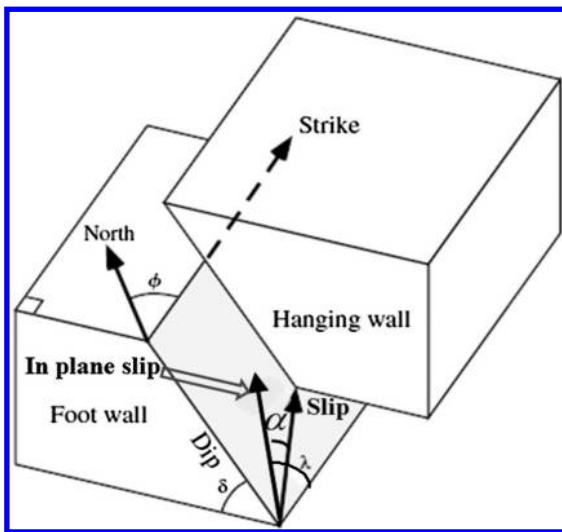

Figure 1. A model for the tensile earthquake (after Aki and Richards, 2002; Vavryčuk, 2011). See the main text for the definition of strike ϕ, dip δ, rake λ, and slope angle α.

The rake λ is measured in the fracture plane as the angle between the strike vector and the projected slip vector. The slope angle α is defined as the inclination of the slip vector from the fracture plane. A positive α indicates a tensile earthquake, whereas a negative α represents a compressive event.

The seismic MT $\mathbf{M}$ for this source in an isotropic (ISO) medium is

$$M_{kl} = \lambda_p v_i n_i \delta_{kl} + \mu(v_k n_l + v_l n_k), \qquad (3)$$

where λ_p and μ are the Lamé coefficients at the focal area (to avoid confusion with fault rake angle λ, the Lamé first parameter is denoted as λ_p in this paper), δ_{kl} is the Kronecker delta, n_l and v_l are the slip vector and fracture plane normal shown in equations 1 and 2, respectively. The symmetric MT $\mathbf{M}$ can be diagonalized and decomposed into double-couple (DC), ISO, and compensated linear vector dipole (CLVD) components,

$$\mathbf{M} = \mathbf{M}^{DEV} + \mathbf{M}^{ISO} = \mathbf{M}^{DC} + \mathbf{M}^{CLVD} + \mathbf{M}^{ISO}, \qquad (4)$$

where

$$M^{ISO} = \frac{1}{3} tr(M) \begin{bmatrix} 1 & 0 & 0 \\ 0 & 1 & 0 \\ 0 & 0 & 1 \end{bmatrix},$$

$$M^{CLVD} = |\varepsilon| \Lambda_{|max|}^{dev} \begin{bmatrix} -1 & 0 & 0 \\ 0 & -1 & 0 \\ 0 & 0 & 2 \end{bmatrix},$$

$$M^{DC} = (1 - 2|\varepsilon|) \Lambda_{|max|}^{dev} \begin{bmatrix} -1 & 0 & 0 \\ 0 & 0 & 0 \\ 0 & 0 & 1 \end{bmatrix},$$

$$\varepsilon = -\frac{\Lambda_{|min|}^{dev}}{\left| \Lambda_{|max|}^{dev} \right|}.$$

Here, $\Lambda_{|max|}^{dev}$ and $\Lambda_{|min|}^{dev}$ are the eigenvalues of the deviatoric MT $\mathbf{M}^{DEV}$ with the maximum and minimum absolute values, respectively. According to Herrmann (1975), the eigenvector $\mathbf{b}$ of the MT matrix $\mathbf{M}$ associated with the intermediate eigenvalue gives the null axis, whereas the eigenvectors $\mathbf{t}$ and $\mathbf{p}$ corresponding to the maximum and minimum eigenvalues give the tension and compression axis, respectively. The fracture plane normal $\mathbf{v}$ and the slip vector $\mathbf{u}$ can be derived from the $\mathbf{t}$ and $\mathbf{p}$ axes after compensating for the nonzero slope angle α (Vavryčuk, 2001) as follows

$$\sin \alpha = 3(\Lambda_{max}^{dev} + \Lambda_{min}^{dev})/(\Lambda_{max}^{dev} - \Lambda_{min}^{dev}), \qquad (5)$$

$$v = \frac{1}{\sqrt{2}}(\sqrt{1 + \sin \alpha} t + \sqrt{1 - \sin \alpha} p), \qquad (6)$$

and

$$n = \frac{1}{\sqrt{2}}(\sqrt{1 + \sin \alpha} t - \sqrt{1 - \sin \alpha} p). \qquad (7)$$

Here, Λ_{max}^{dev}, Λ_{min}^{dev} denote the maximum and minimum eigenvalues of the deviatoric MT $\mathbf{M}^{DEV}$. Based on equations 1, 2, 5, 6, the source parameters, slope angle α, strike ϕ, dip δ, and rake λ could be determined from the MT M. The ratio between the Lamé coefficients λ_p and μ at the focal area is another source parameter, defined as k and can be derived from the MT M as follows

$$k = \lambda_p / \mu = \frac{2}{3} \left(\frac{tr(M)}{\Lambda_{max}^{dev} + \Lambda_{min}^{dev}} - 1 \right). \qquad (8)$$

According to Vavryčuk (2001), the stability conditions imposed on an ISO medium requires

$$k = \lambda_p / \mu > -\frac{2}{3}, \qquad \mu > 0. \qquad (9)$$

This also poses a lower limit for the V_P/V_S ratio at the focal area of the earthquakes that follow the tensile earthquake model,

$$V_P / V_S = \sqrt{k + 2} > 1.15. \qquad (10)$$

According to this limit, all measurable physical properties in the focal area including V_P, V_S, the bulk modulus, and the shear modulus are positive.

Other source parameters including seismic moment M_0, MT magnitude M_w, and DC, ISO, and CLVD component percentages could also be determined from the MT (Vavryčuk, 2001; Song and Toksöz, 2011).

Full-waveform based source mechanism determination using dual-array data

In this paper, we adopt the full-waveform inversion approach of Song and Toksöz (2011) to determine the complete MT of microseismic events in the Barnett Shale.

To reduce the influence from errors in source locations, during the MT inversion, we perform a grid search around the initial source location (Song and Toksöz, 2011). The spatial search range and grid size are selected based on the location uncertainty. The location uncertainty in the downhole monitoring scenario is estimated from the standard deviations of P- and S-wave arrival times and P-wave polarization angles (Eisner et al., 2010). For the dual-array data set used in this study, we calculate standard deviations and obtain 4.6 m (15 ft) in the radial direction, 7.6 m (25 ft) in the vertical direction and 2° in P-wave derived event back-azimuths constrained by two geophone arrays. We further determine the location uncertainty in the horizontal directions (north and east) from the standard deviations of the radial distances and P-wave derived event back-azimuths at a typical distance of 305 m (1000 ft) for the selected 42 events. The standard deviation is estimated to be 10.6 m (35 ft). Therefore, a spatial grid size of 3 m (10 ft) and a spatial search cube with the size of $7 \times 7 \times 5$ grids (north, east, and down) are used throughout this paper.

In this study, we match full waveforms from geophone arrays deployed in two vertical wells. In principle, complete MT can be extracted from two observation wells for any event not situated on the observation well plane. As pointed out by Eaton and Forouhideh (2011), in a homogeneous medium, the condition number of the sensitivity matrix for MT inversion is inversely proportional to the solid angle at the source subtended by the geophone array. The nondirect waves propagated through a layered medium increase the source take-off angle coverage and, therefore, reduce the condition number (Song and Toksöz, 2011). In either case, an azimuthal angle at the source subtended by two vertical geophone arrays close to 90° is desirable to assure a low condition number. Therefore, in this paper, we select several events that have good S/Ns in P- and S-waves and azimuthal angles to the two geophone arrays close to 90°.

In this study, there was a significant difference in noise standard deviations from geophones at different wells. Thus, a weighted least-squares inversion is performed inside the grid search loop of event location and origin time. The weights are determined from the pre-event noise standard deviation at each geophone, for each component. The weight for the n-th geophone, i-th component, w_{ni}, is calculated as the inverse of the preevent noise standard deviation at the corresponding channel

$$w_{ni} = 1/\mathrm{std}(n_i(x_r^n, t)), \tag{11}$$

where $n_i(x_r^n, t)$ is the ith component data of the preevent noise at nth geophone.

The best solution of the event location x_s, origin time t_0, and MT $M_l(l = 1, 2, \ldots, 6)$ is determined by minimizing the squared L-2 norm of the weighted waveform fitting error:

$$J(x_s, t_0, M_l) = \sum_{k=1}^{N_t} \sum_{n=1}^{N} \sum_{i=1}^{N_c} w_{ni}^2 (d_i(x_r^n, k\Delta t) - v_i(x_r^n, x_s, k\Delta t))^2. \tag{12}$$

Equivalently, the grid-search based complete MT inversion is meant to maximize the variance reduction VAR, defined as

$$\mathrm{VAR}(x_s, t_0, M_l) = 1 - J(x_s, t_0, M_l). \tag{13}$$

It is worth noting that other forms of measures such as the cross-correlation between modeled and observed data could be used to gauge the goodness of fit (Kawakatsu and Montagner, 2008; Li et al., 2011). The choice of equation 12 as the objective function is based on the fact that only events with good S/Ns in P- and S-waves are considered in this study. Therefore, both P- and S-waves will contribute to the minimization of $J(x_s, t_0, M_l)$. This may introduce a possible event selection bias. However, the chance of having both geophone arrays situated in P-wave nodal planes is low. Moreover, the location of microseismic events also requires good P-waves from at least one geophone array.

Because the vertical component data display a poor S/N, only horizontal components are used in the inversion. The reasons for the poor S/Ns associated with the vertical component may come from two sources (Song and Toksöz, 2011). First, vertical component geophones are normally harder to couple into the formation compared to horizontal component geophones in a vertical bore-

hole. Second, surface noise such as pumping and culture noise coupled into the borehole propagates as guided wave modes like Stoneley-waves, which have predominant motion in the vertical component.

FIELD STUDY

An overview of the Barnett gas shale reservoir

During the Mississippian, the Fort Worth Basin was bordered on its outboard side by an island-arc system which supplied very little coarse-grained sediment to the Barnett Shale. Limestone interbeds in the Barnett (including the middle Forestburg Member) formed as mass-gravity or turbidity flows of skeletal material derived from surrounding carbonate platforms. Immediately after black-shale deposition, a temporary expansion of the western carbonate produced the overlying Marble Falls Formation. The Mississippian stratigraphic section in the Fort Worth Basin consists of limestone and organic-rich shale. The Barnett Shale formation, in particular, consists of dense, organic-rich, soft, thin-bedded, petroliferous, fossiliferous shale and hard, black, finely crystalline, petroliferous, fossiliferous limestone (Lancaster et al., 1993).

The Barnett Shale, as determined by core and outcrop studies, is dominated by clay- and silt-size sediment with occasional beds of skeletal debris. In lithologic descriptions, the Barnett Shale is a mudstone rather than shale. It is highly indurated, with silica making up approximately 35%–50% of the formation by volume and clay minerals less than 35% (Bruner and Smosna, 2011). This silica-rich nonfissile shale behaves in a more brittle fashion and fractures more easily than clay-rich shales, responding well to stimulation.

The Barnett Shale reservoir has characteristic features of very low matrix permeability in the range of microdarcies to nanodarcies (Johnston, 2004), and some degree of natural-fracture development (Bruner and Smosna, 2011). From core studies, two major sets of natural fractures were identified. One fracture system had an azimuth of north–south (north–south) and another, west-northwest–east-southeast (west-northwest) (Gale et al., 2007; Gale and Holder, 2010). The natural fractures in the Barnett Shale are completely healed and filled with calcites.

Field setup

A microseismic survey using two vertical wells at a separation of approximately 487 m (1600 ft) was conducted during the waterfrac treatment of the Barnett Shale in the Fort Worth Basin at depths of approximately 2290 m (7500 ft). Each observation well had twelve 3C geophones spaced approximately 12 m (40 ft) apart, with the tool situated just above the shale interval that was being stimulated. The microseismic data were recorded at a sample frequency of 4 KHz. The recorded data were analyzed and located for hydraulic fracturing mapping as outlined by Warpinski et al. (2005). The velocity model for location, shown in Figure 2a, was derived from the well-logging data and calibrated using perforation shots. Information on local geology was also considered when building the velocity model.

A typical anisotropy parameter for the Barnett Shale is reported as $\varepsilon = 0.1, \Delta = 0.2, \gamma = 0.1$ (note that the Thomsen parameter which controls the near-vertical anisotropic response is denoted as Δ in this paper to avoid the confusion with fracture dip angle

δ) (Warpinski et al., 2009). The raypaths are mostly horizontal, with a maximum deviation from the horizontal less than 22° (Warpinski et al., 2009). According to Thomsen (1986), the P-wave velocity variation from the horizontal direction is less than 2%, while the SH velocity variation is less than 1.5%. Therefore, we may conclude that, for this data set, the effect of anisotropy on the waveform modeling is small relative to the general uncertainty in velocity. In the study, the perforation-calibrated horizontal velocity model described in Figure 2a is used and the anisotropy effect is neglected. Table 1 lists the seismic properties of the layer sequence in the Barnett Shale reservoir, which are used to generate synthetic seismograms for MT inversion. The density information is extracted from the density log. The P- and S-wave Q-factor values at each layer are taken from values compiled by Toksöz and Johnson (1981) for the corresponding lithology type. The Qp and Qs values are further calibrated based on the average amplitude decay measured across the geophone arrays (Rutledge et al., 2004).

Figure 3 gives the horizontal plane view of the microseismic event locations from waterfrac treatment in the Barnett Shale using the ISO velocity model shown in Figure 2a. Most of the microseismic events occur in the lower Barnett Shale interval. The two vertical observation wells 1 and 2 are presented as the yellow and green squares on Figure 3, respectively. The green dashed line represents the observation well plane. We select 42 events that have good S/Ns and azimuthal angles to the two geophone arrays close to 90° for complete MT inversion. Among the chosen events, four spatial clusters appear and are denoted as G1, G2, G3, and G4, respectively.

Events with similar locations have similar condition numbers. Therefore, in the following section, we will conduct a systematic study to evaluate the uncertainty of the source parameters derived from full-waveform based MT inversion for each event group using synthetic data. After that, we will proceed to the geomechanical analysis section to gain some insights on how microearthquakes are generated. Finally, we will discuss the field study results.

Uncertainty of the inverted source parameters from synthetic study

First, we study the influence of data noise and source mislocations by performing a Monte Carlo test. In this test, we generate noise-free synthetic seismograms for each example event within the four event groups using the reference velocity model shown in Figure 2a to mimic the field case. Without losing generality, four tensile earthquakes with (ϕ, δ, λ, α, k) of (60°, 80°, 60°, 20°, −0.3), (30°, 75°, −160°, 15°, 0.8), (55°, 85°, 80°, 25°, −0.5), and (10°, 50°, 75°, −20°, 0.1) were simulated to represent events in group G1, G2, G3, and G4, respectively. The DC component percentages for each of these four tensile earthquakes are 53%, 51%, 48%, and 48%. The same source model is used throughout the synthetic study section. It is worth noting that a larger slope angle α is chosen with a higher dip δ in this model. The motivation for this choice will be further illustrated in the geomechanical analysis section.

For each well, the noisy synthetic data were formed by adding zero-mean Gaussian noise with a standard deviation reaching 10% of the absolute maximum amplitude of the two horizontal components averaged across the twelve geophones. The noise was added independently for each geophone array at the same noise level of 10%. The noise level of 10% was set to represent the estimated noise level in the field data set.

To investigate the influence of source mislocations, the true event location is randomly perturbed up to 10.6 m (35 ft) in each horizontal direction and 7.6 m (25 ft) in the vertical direction to represent the location uncertainty in the field example. In the inversion, a grid search is carried out around the perturbed event location. The MT inversion is performed on the [100, 300] Hz band-pass filtered noisy synthetic data using the correct velocity model. The source parameters are estimated from the inverted complete MT. In all synthetic tests, we distinguish the fracture plane from the auxiliary plane by selecting the one with a smaller deviation from the true fracture orientation. However, in the field study, where no knowledge about the true source parameters is available, we will propose a method to distinguish the fracture plane from the
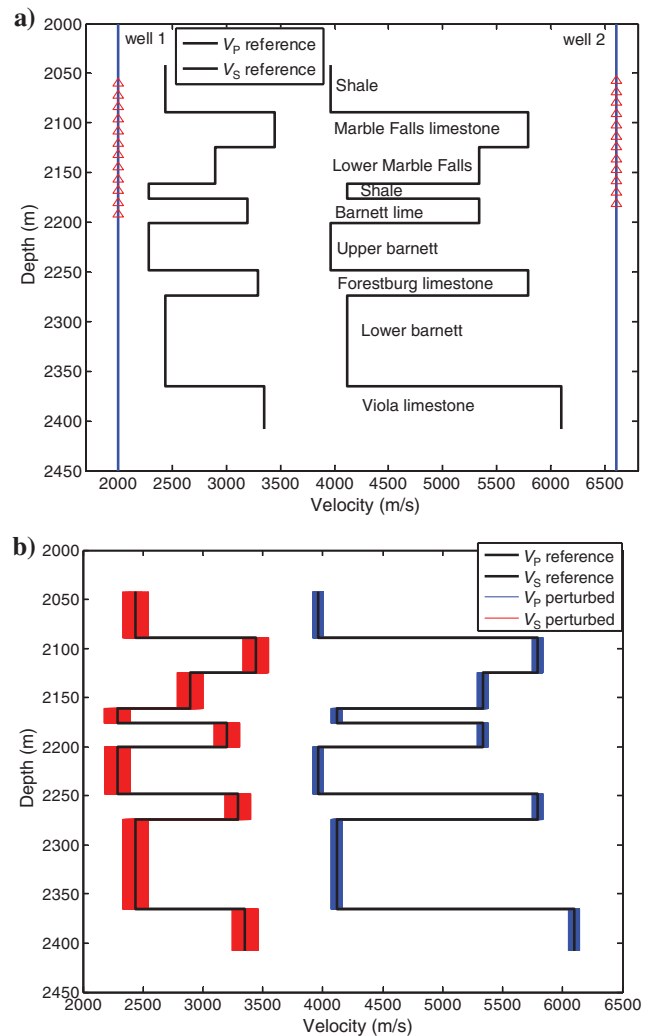

Figure 2. (a) One-dimensional P- and S-wave velocity model derived from the field study shown in the black. The blue lines on the left and right sides denote the observation wells 1 and 2, respectively. The red triangles represent the depth of the 12 geophones in each observation well. The rock type for each layer is also listed in the figure. The waterrefrac treatment is performed in the lower Barnett interval, with most of microseismic events occurring also in the lower Barnett interval. (b) The darken red lines and blue lines depict the perturbed P- and S-wave velocity models to study the influence of velocity model errors on the inverted source parameters.

auxiliary plane according to the insights from the geomechanical analysis.

To obtain statistically relevant results, we perform 100 MT inversions and source parameter estimations, each with a different noise realization. Table 2 summarizes the average absolute errors of the inverted source parameters for four example events together with the corresponding condition numbers. The example event G4 has the largest condition number due to the smallest azimuthal angle at G4 subtended by the two geophone arrays, which is seen on Figure 3. Overall, the inverted source parameters agree well with the true values, with average absolute errors in FPS and slope angle α less than 2°. The average absolute errors in component percentages, k and M_0 are also negligible. This indicates that with a correct velocity model, microseismic source mechanisms can be reliably determined from the dual-array data set by the grid-search based full-waveform inversion approach, as long as the event mislocation is within the location uncertainty and the condition number is reasonably low. Additive data noise has a minimal effect on the inversion, which is also reported in Song and Toksöz (2011). It is interesting to point out that, at the same noise level, errors in the inverted source parameters tend to be higher at a larger condition number. This is reasonable, because the errors propagated into the MT solution from data noise are controlled by the condition number.

Next, we perform the DC inversion instead of complete MT inversion on the same band pass-filtered noisy synthetic data. In this inversion, the event source mechanism is forced to be DC. Therefore, it provides no information on α, k, and component percentages. Table 3 lists the average absolute errors of the inverted seismic moment and FPS for four example events. Compared to Table 2, it is clear that DC inversion severely biased the estimates of fracture plane orientation even with a correct velocity model. This is understandable, because the DC source clearly is not a good assumption about the underlying tensile earthquakes, which have a DC component percentage of only about 50%.

Finally, we investigate the influence of velocity model errors on the inversion. In this test, the P- and S-wave velocity models are randomly perturbed up to 10% and 20% of the velocity difference between adjacent layers so that the sign of the velocity difference between adjacent layers does not change. A larger perturbation in S-wave velocity is to take into account the fact that the S-wave velocity is generally less reliably determined than the P-wave velocity. The perturbation is independent between different layers and P- and S-wave velocities are independently perturbed. The density model is kept unchanged, as the velocity perturbation is dominant in determining the characteristics of the waveforms. The Qp and Qs model is also kept fixed to study the influence of the velocity perturbation. The velocity models are perturbed 100 times, as shown in Figure 2b. We then conduct 100 MT inversions and source parameter estimations, each with a different velocity model and noise realization. In each inversion, the 10% Gaussian noise and the same amount of source mislocations as the case for Table 2 are also included.

Figure 4 shows the best waveform fitting of the synthetic event G1 for one velocity model and noise realization. A good agreement between modeled data in black and band-pass filtered synthetic data in red is seen on both components. One hundred MT inversions, each with one inaccurate velocity model and noise realization, are performed to study the influence of velocity model errors on the inverted source parameters. Figure 5 plots the errors of the inverted event location along (north, east, and down) directions in stars for the synthetic tensile source G1 as a function of different velocity model realizations. The event location error is shown as multiples of search grid size. The black line represents the search limit in the vertical direction for the grid-search based MT inversion, whereas the green line demonstrates the identical search limit in the north and east directions. It is observed that all the location errors are bounded in the search limit. This indicates that our search range is sufficient for the assumed velocity model errors. Figure 6 gives the histograms of errors in the inverted source parameters for the synthetic event G1. Likewise, Figure 7 plots the histograms of errors in the inverted source parameters for the synthetic event G4.

A similar Monte-Carlo test was also conducted for synthetic events G2 and G3. Table 4 summarizes the average absolute errors of the inverted source parameters for all four synthetic events. The median value of the condition number of the inversion matrix across the 100 inversions is also listed for each example event. Three observations are seen in Table 4. First, compared to Table 2, the errors

Table 1. Seismic properties of the layer sequence in the Barnett Shale gas reservoir. The P- and S-wave velocities are calibrated by perforation timing. Q_p and Q_s values are determined from the lithology and amplitude decay measured across the geophones (Toksöz and Johnson, 1981; Rutledge et al., 2004)

Layer number (Rock type)	Property				
	V_P (Km/s)	V_S (Km/s)	ρ (g/cm³)	Q_p	Q_s
1 (Shale)	3.96	2.44	2.4	100	60
2 (Marble Falls limestone)	5.79	3.44	2.6	200	100
3 (Lower Marble Falls)	5.33	2.90	2.6	200	100
4 (Shale)	4.11	2.29	2.4	100	60
5 (Barnett lime)	5.33	3.20	2.65	200	100
6 (Upper Barnett Shale)	3.96	2.29	2.55	100	60
7 (Forestburg limestone)	5.79	3.29	2.7	200	100
8 (Lower Barnett Shale)	4.11	2.44	2.5	100	60
9 (Viola limestone)	6.09	3.35	2.65	200	100

in the inverted source parameters are clearly increased for all events. This signifies that the velocity model errors have a more profound influence in the MT inversion than data noise and source mislocations. Secondly, at the same noise level and with the same amount of velocity model perturbations, the example event with the smallest median condition number (event G3) tends to have the least error in source parameter estimates. For the assumed velocity model errors, the event G1, with the largest condition number, has an average absolute error of 0.9, 14°, 22°, and 21% for k, α, ϕ, and CLVD
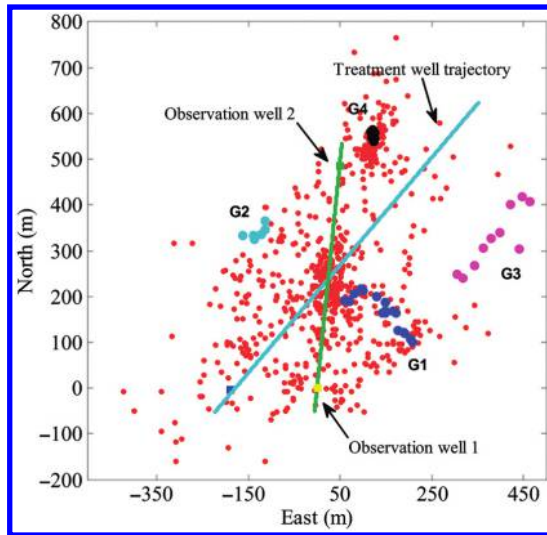

Figure 3. Horizontal plane view of the microseismic event locations from waterfrac treatment in the Barnett Shale plotted as red circles. The yellow and green squares denote the two vertical observation wells 1 and 2, respectively, while the treatment well trajectory is plotted as the cyan line with treatment wellhead shown as the blue square. The origin (0, 0) corresponds to the location of observation well 1. The green dotted line represents the observation well plane. A total of 42 events located off the observation well plane with good S/Ns are selected for source mechanism study in this paper. Among the selected events, four spatial clusters are seen and denoted as G1, G2, G3, and G4, respectively.

component percentage, respectively. Finally, among all four inverted source parameters (ϕ, δ, λ, α) related to the fracture plane orientation and slip direction, the dip angle δ is the most reliably determined, with a maximum error up to 5°, and the strike angle ϕ is the least accurate estimate. The errors in the inverted slope angle α are also small, indicating that α can be accurately estimated.

Hydraulic fracture geomechanics in the Barnett Shale

Microseismicity associated with hydraulic fracturing has considerably different geomechanical aspects than tectonic earthquakes, rockbursts, or geothermal shear dilation. The inflation of a hydraulic fracture with internal pressure induces very large stresses in the surrounding formation. The stress perturbations are often greater than the stress difference that existed in the formation prior to fracturing. In addition, the leakoff of the high pressure fluid, at pressures well above the minimum in situ stress, reduces the normal stress, and destabilizes any natural fractures or other permeable weakness planes. These combined factors create the unstable zones around the hydraulic fracture where the microseismicity would occur (Warpinski et al., 2012). In this section, we calculate the hydraulic-fracture-induced stress perturbations in the Barnett Shale and consider

Table 3. Statistics of DC inversion. The inversion is performed on the same noise-contaminated synthetic data as Table 2 and uses the correct velocity model and the mislocated source.

Mean absolute errors in the inverted source parameters	Example event			
	G1	G2	G3	G4
Seismic moment (%)	12	6	27	40
Strike (°)	61	37	3	60
Dip (°)	38	8	4	4
Rake (°)	49	160	29	56

Table 2. Statistics of complete MT inversion performed with 10% Gaussian noise contaminated synthetic data and the correct velocity model and the mislocated source. The corresponding condition number of the inversion matrix is listed below the event ID.

Mean absolute errors in the inverted source parameters	Example event (condition number)			
	G1(18)	G2(9)	G3(17)	G4(20)
Seismic moment (%)	2.8	0.5	0.7	1.5
$k = \lambda_p/\mu$	0.05	0.04	0.01	0.01
Slope (°)	0.5	0.4	0.4	0.5
Strike (°)	1.5	0.4	0.1	0.4
Dip (°)	0.6	0.3	0.1	0.2
Rake (°)	0.4	0.5	0.5	0.2
DC component percentage (%)	1.3	0.5	0.7	0.9
ISO component percentage (%)	1.4	0.2	0.2	0.2
CLVD component percentage (%)	0.8	0.5	0.5	0.7

the pore pressure increase resulting from fracturing fluid leakage to study possible failure types that could occur in the Barnett Shale.

Looking at a single hydraulic fracture for simplicity, there are several models available to calculate the stress field induced by the fracture, including finite element and analytical models. Among the various analytical models, the most versatile one is a pressurized 3D elliptic crack (Green and Sneddon, 1950). This model requires a homogeneous, ISO, linear-elastic formation and a uniform fluid pressure inside the hydraulic fracture, but these simplifications still allow for adequate evaluation of the characteristics of the stress field
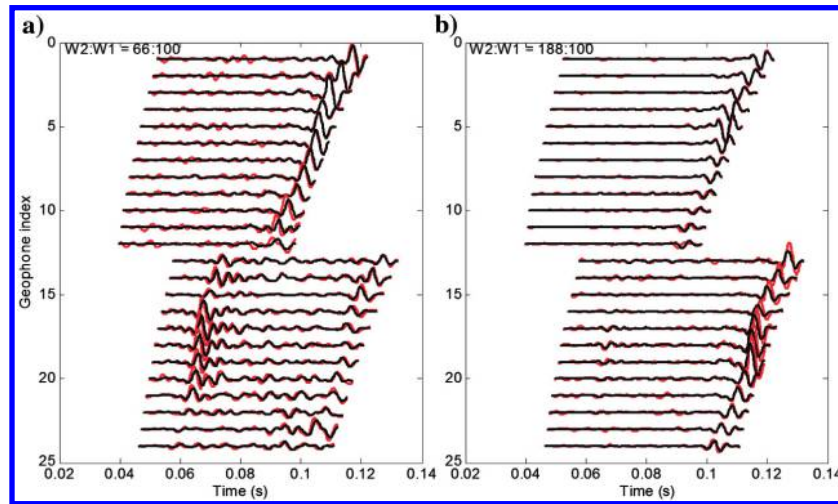

Figure 4. Comparison between the modeled data in black and band-pass filtered noisy synthetic data in red for the synthetic tensile event G1. (a) North; (b) east component plot. The relative scaling factors between well 1 (geophones 1–12) and well 2 (geophones 13–24) are listed. In this test, 10% Gaussian noise is added to the noise-free data of the synthetic tensile event G1 to form the noisy synthetic data for inversion. The complete MT inversion is performed on the filtered horizontal component data with an inaccurate velocity model and event location. The modeled data are generated from the inverted microseismic MT matrix (six independent elements).
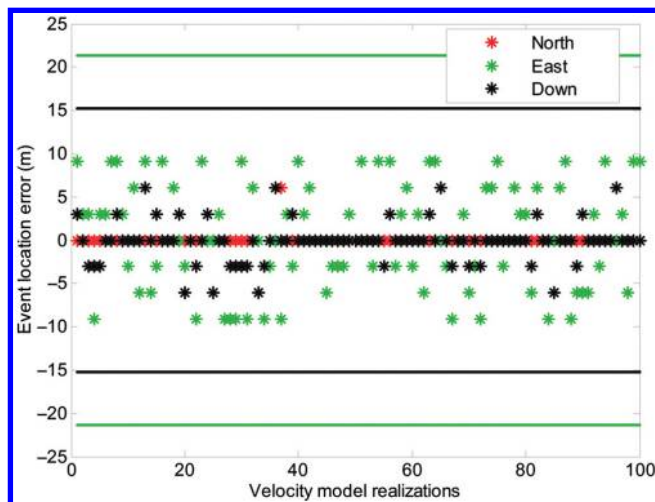

Figure 5. The errors of the inverted event location in (north, east, and down) directions for the synthetic tensile source G1 (stars) as a function of velocity model realizations. The black line shows the search limit in the vertical direction in the grid search, whereas the search limit in the north and east directions is identical and plotted as the green line.

around the hydraulic fracture and the influence of the stress field on rock failure behavior. As described in Figure 8a, the stress perturbations have two characteristic zones: a tip-influenced region along the hydrofracture tip direction and a broadside region along the hydrofracture normal direction, and these are considered separately. Prior to fracturing, the Barnett Shale reservoir is in the normal faulting regime (Bruner and Smosna, 2011; Agarwal et al., 2012). Therefore, the broadside region is expected to be parallel to the unperturbed minimum horizontal principal stress (Shmin) direction and the tip region is oriented in the direction of the unperturbed maximum horizontal principal stress (SHmax) direction. Only a vertical fracture is considered here.

Table 5 lists the hydrofracture and formation parameters typical of the Barnett Shale waterfrac treatment (Agarwal et al., 2012). The broadside region, the area alongside the hydrofracture after the tip has passed, can be assessed using the analytic model of Green and Sneddon (1950) for typical elongated fractures (length > height). Figure 8b gives the stress decay moving away from the hydrofracture face along the centerline of the hydrofracture, with respect to length and height. The largest stress perturbation is the compressive stress along the Shmin direction. Although the stress perturbation in the SHmax direction is also compressive, it is considerably less. This behavior suggests the stress perturbations imposed by the hydrofracture are highly stabilizing in the broadside region. The reason is twofold. First, the shear stress in the formation is significantly reduced because the horizontal differential stress is decreased after the hydrofracture perturbation. Second, the total normal stress is increased, because compressive stress is added to SHmax and Shmin stresses. The combined effect is to increase frictional strength and reduce the available shear stress, making it very difficult for microearthquakes to occur. One possibility to generate microseismicity in the broadside region is to have the high-pressure fracturing fluid leak off into permeable weak zones such as natural fractures, because the increase in the pore pressure from fluid leakage will destabilize the weak zones and cause microearthquakes to happen (Warpinski et al., 2012). For an overpressured gas reservoir such as the Barnett Shale reservoir, the pore pressure increase resulting from fracturing fluid leakage is actually much greater than the stress perturbation due to the opening of the hydrofracture, because the pore pressure change is on the order of the fracturing pressure minus the ambient pore pressure, but the stress change, i.e., the net pressure, is on the order of the fracturing pressure minus the unperturbed Shmin stress.

The tip region of the hydrofracture has a different stress perturbation pattern. Figure 8c plots the stress perturbations due to the presence of the hydrofracture ahead of the length tip along the centerline of the hydrofracture with respect to height and width. Here, all the stress changes are tensile. The largest tensile stress is along the SHmax direction, and a slightly smaller tensile stress occurs along the Shmin direction. This has the effect of slightly decreasing the horizontal differential stress and significantly decreas-

ing the total stress. The net effect could be destabilizing the tip region and inducing microearthquakes if any favorably oriented weakness planes are encountered. This zone is relatively small, at most a few meters, and provides a mechanism for microearthquakes to occur slightly ahead of the hydrofracture tip. In contrast to the broadside region, no fluid leakage is expected in this zone, and therefore the pore pressure stays as the ambient pore pressure.

The above calculations are related to a single hydraulic fracture. Although the geomechanics become considerably more complex in the case of multiple hydraulic fractures during the multiple-stage, multiple-perforation treatment, the general features of stress perturbations from the single hydraulic fracture analysis still hold (Agarwal et al., 2012; Warpinski et al., 2012).

Fischer and Guest (2011) have proposed a way to identify four different types of earthquakes as shown in Figure 9: pure tensile ($\sigma_n < 0, \tau = 0, \alpha > 0$) and hybrid tensile ($\sigma_n < 0, |\tau| > 0, \alpha > 0$; hybrid tensile events will be called tensile events hereafter), pure shear ($\sigma_n = 0, |\tau| > 0, \alpha = 0$), and compressive shear ($\sigma_n > 0, |\tau| > 0, \alpha < 0$) events. The Mohr circle was used to represent in situ stress state, and the Griffith failure criterion was adopted to describe shear and tensile failures (Ramsey and Chester, 2004). The Griffith failure criterion reads

$$\tau^2 = 4T_0(\sigma_n + T_0), \qquad (14)$$

$$S_0 = 2T_0, \qquad (15)$$

where S_0 and T_0 are the inherent cohesion strength and the tensile strength of the rock. According to the Griffith failure criterion, rock will fail along a fracture plane where the shear stress τ reaches the level specified by equations 14.

Only the fluid leakage effect was considered by Fischer and Guest (2011). However, the stress perturbations from the hydrofracture are important for the analysis of microseismicity associated with hydraulic fracturing (Warpinski et al., 2012). In this study, we take into account the fluid leakage effect and stress perturbations due to the presence of the hydrofracture. We consider two possibilities, microseismicity occurring in the intact rock and on the weak zones such as natural fractures and induced hydraulic fractures.

Different cohesion strength values were proposed to describe the intact rock and the weak zones inside the Barnett Shale. The cohesion strength is normally derived from the tensile strength according to equations 15. It is generally accepted that the tensile strength value is highly variable. In Gale and Holder (2008), a tensile strength value ranging from 12 to 44 MPa was reported for the Barnett Shale samples tested,

while in Tran et al. (2010), a tensile strength value of the Barnett Shale ranging from 1.38 MPa (200 psi) to 20.7 MPa (3000 psi) was proposed. In this study, we found that a tensile strength of 10 MPa for the intact rock and 1 MPa for the weak zones inside the Barnett Shale seems to adequately explain the observed microseismicity. The core analysis indicates that the natural fractures inside the Barnett Shale are calcite-filled whereas the rock matrix is mostly
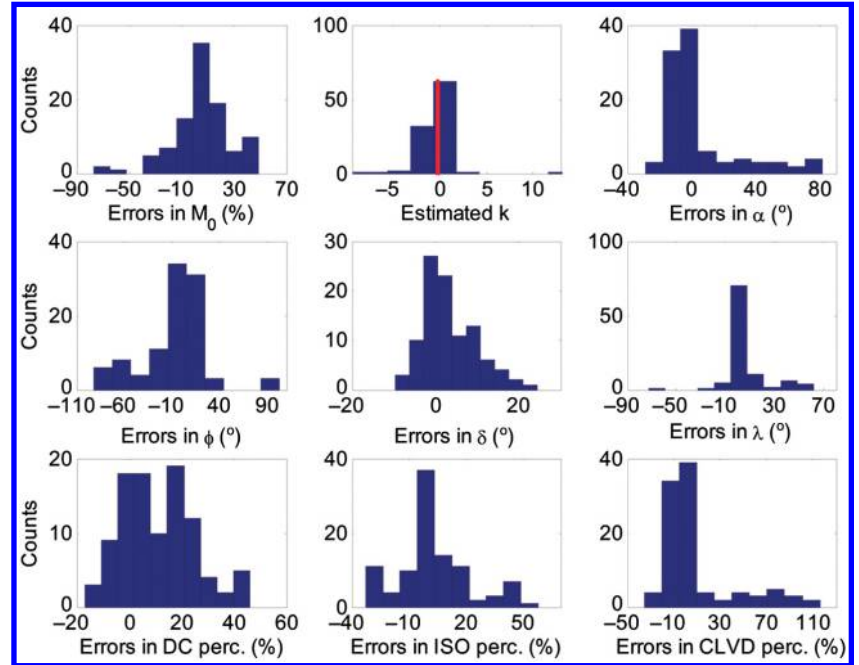

Figure 6. The histograms of errors in the inverted source parameters for the synthetic tensile source G1.
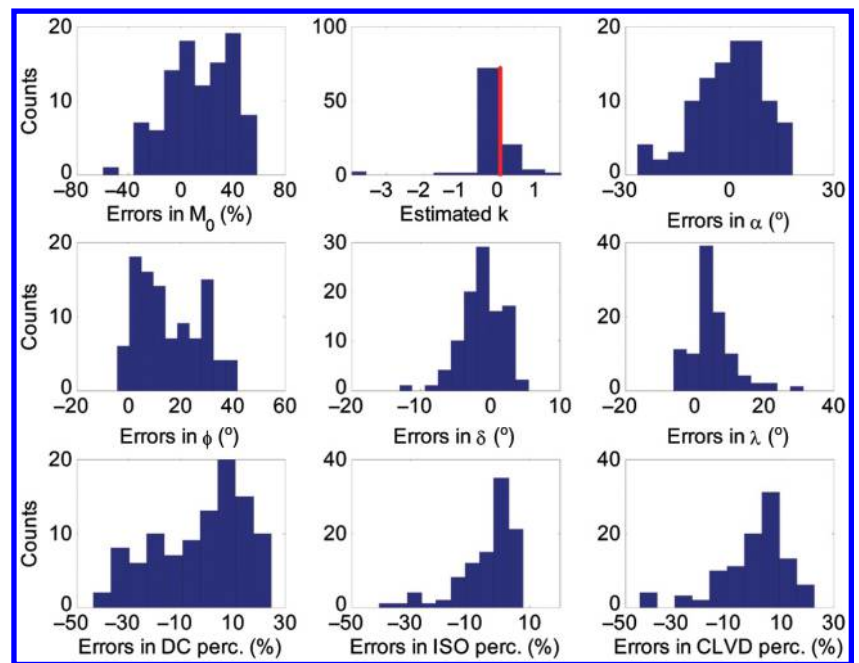

Figure 7. The histograms of errors in the inverted source parameters for the synthetic compressive source G4.

Table 4. Statistics of complete MT inversion. The inversion is performed on the same noise-ontaminated synthetic data as Table 2 and uses an approximate velocity model and mislocated source. Different additive noise realizations are used for different velocity model realizations. The true MTs for the example event in each event group are identical to those of Table 2. The median condition number of the inversion matrix among 100 different velocity model realizations are listed below the event ID.

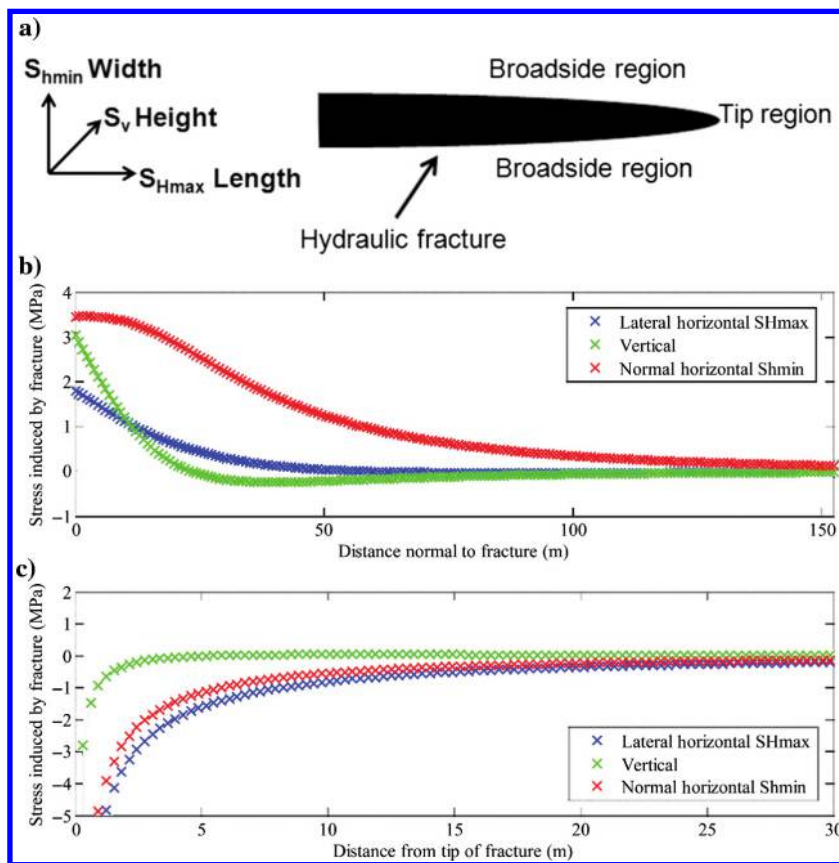| Mean absolute errors in the inverted source parameters	Example event (condition number)			
	G1 (23)	G2 (6)	G3 (4)	G4 (17)
Seismic moment (%)	17	15	13	24
$k = \lambda_p/\mu$	0.9	0.4	0.1	0.3
Slope (°)	14	3	3	8
Strike (°)	22	7	2	16
Dip (°)	5	3	2	3
Rake (°)	9	7	5	6
DC component percentage (%)	14	4	5	14
ISO component percentage (%)	14	4	3	7
CLVD component percentage (%)	21	4	4	10

Figure 8. The stress perturbations due to a 3D elliptic hydraulic fracture. (a) The horizontal plane view of the 3D elliptic hydraulic fracture model and its characteristic stress perturbation regions. The out of the paper direction is the vertical (fracture height) direction. Two characteristic neighborhood regions: tip region and broadside region, are classified according to the different features of stress perturbations induced by the 3D elliptic hydraulic fracture. (b) Stress decay normal to fracture face along centerline of fracture in the broadside region. (c) Stress decay ahead of the length tip along centerline of fracture in the tip region.

siliceous, suggesting a weak bond between the calcite filling and the surrounding rock matrix (Gale et al., 2007). Therefore, one tenth of the tensile strength of the intact rock is assigned as the tensile strength of the natural fractures in this study. The difference between the tensile strength of the intact rock used in this paper and that reported by Gale and Holder (2008) may be attributed to the scale effect and possible data selection bias in the laboratory study. The observed microseismicity typically occurs at a much larger scale than the size of core samples used in the laboratory test. Moreover, stronger rock samples with higher tensile strengths are easier for laboratory testing, and thus may incur the data selection bias. Overall, the parameters used for geomechanical analysis of the Barnett Shale are listed in Table 5.

In Figure 10a, the 3D Mohr-circle illustrates the stress state in the Barnett Shale (Zoback, 2007). The blue circle on the right corresponds to the case of the ambient pore pressure p_0, while the left circle is associated with the maximum possible pore pressure case, that is, when the pore pressure is elevated to the fracturing pressure p_f. The Griffith failure envelope for the intact rock with the inherent cohesion strength S_0 of 20 MPa is plotted in Figure 10a as the red curve. It is discovered that even at the maximum possible pore pressure, rock failure is very unlikely to occur in the intact rock because of its large cohesion strength. It is worth mentioning that in Figure 10a only the pore pressure effect is considered, because the pore pressure increase resulting from fracturing fluid leakage could potentially be much greater than the stress

perturbation due to opening of the hydrofracture under the treatment parameters listed in Table 5.

Figure 10b gives the failure analysis in the tip region. In this region, it is assumed that no fracturing fluid leakage occurs. According to Figure 8, the stress perturbations due to the hydraulic fracture are assumed to be $-0.77p_{net}$, $-p_{net}$, and $-0.1p_{net}$ along the Shmin, SHmax, and vertical directions, respectively. The black, green, and cyan crosses denote the principal stresses in the original unperturbed Shmin (northwest–southeast), SHmax (northeast–southwest), and vertical directions, respectively. It is interesting to see that the relative magnitude of the Shmin and SHmax principal stresses has changed due to the stress perturbation from the hydraulic fracture. The original Shmin (northwest–southeast) direction is now becoming the maximum in situ horizontal stress direction. The Griffith failure envelope for the weak zones inside the Barnett Shale with the inherent cohesion strength S_{0w} of 2 MPa is plotted as the red curve. It is found from Figure 10b that compressive shear events could happen on some preferred weak zones in the tip region. As described in Figure 10b, at the failure point, the angle between the fracture plane normal and the maximum principal stress direction (the vertical direction in the Barnett Shale case) is equal to 2δ, that is, twice the fracture dip (Zoback, 2007). This suggests that compressive shear events ($\alpha < 0$) at a dip around 50° could occur on weak zones such as natural fractures in the tip region. This result may sound counterintuitive, but the overall compressive stress condition after hydraulic fracturing treatment prevents tensile failures. One possibility for microearthquakes to occur under the compressive stress condition in the tip region is asperity shearing (Warpinski, 1991). Shearing on the rough surfaces of natural fractures could cause a reduction in volume and therefore induce a crack closure component. The shear strength in this region is reduced by the asperity shearing process, which may allow additional shearing to occur.

Figure 11a presents the failure analysis in the broadside region. The stress perturbations from the hydraulic fracture are assumed to be $+0.5p_{net}$, $+0.1p_{net}$ and zero in the Shmin, SHmax, and vertical directions, respectively. The decrease of horizontal differential

stress, together with the increase in the total stress, stabilizes the broadside region. Therefore, the fracturing fluid leakoff into the weakness zones is essential for microearthquakes to occur in this region. The pore pressure increase is assumed to be equal to the net fracturing pressure p_{net} minus a pressure drop term. The pressure drop is inversely proportional to the square root of the permeability of the natural fractures, which is unknown. In Figure 11, a pressure drop of 200 psi is assumed, as suggested by Agarwal et al. (2012). The selection of this value is not intended to estimate the pressure drop but to serve as a scoping parameter. The black, green, and cyan crosses denote the principal stresses along the original unperturbed Shmin (northwest–southeast), SHmax (northeast–southwest), and vertical directions, respectively. The interchange of Shmin and SHmax directions resulting from the hydrofracture induced stress changes is also seen. The red, green, and blue pluses demonstrate the shear and effective normal stresses on the fracture planes with strike angles of (80°, 140°), (10°, 70°), and (−15°, 45°), respectively (corresponding to a ±30° range around the west-northwest, northeast–southwest, and north–south directions). The corresponding dip angles are also listed in the figure. The Griffith failure envelope for the weak zones with the inherent cohesion strength S_{0w} of 2 MPa is plotted as the red curve. It is observed in Figure 11a that compressive shear and tensile events could happen on some preferred fractures in the broadside region with the existence of fluid leakage. Similar to Figure 10, because of the decreased horizontal differential stress after hydrofracture stress perturbation, the 3D Mohr circle behaves like a 2D Mohr circle with almost identical principal stresses in Shmin and SHmax directions. Therefore, for reservoirs with a low horizontal differential stress and in normal faulting regimes, such as the Barnett Shale reservoir, rock failure could occur along almost any strike direction. However, the fracture plane dip angle does play an important role in determining the failure type. Figure 11b gives the zoomed version of Figure 11a. It is clear that, in spite of different strike angles, tensile events could only occur at high dip angles such as $\delta = 80°$ in this figure, whereas compressive shear events are observed at a low dip angle like $\delta = 45°$.

Table 5. Parameters for a typical waterfrac treatment in the Barnett Shale taken from (Agarwal et al., 2012).

| Parameter	Value
Hydraulic fracture half-length x_f	150 m (492 ft)
Hydraulic fracture height h_f	60 m (197 ft)
Young's modulus, E	45 GPa (6.53×10^6 psi)
Poisson's ratio	0.2
Minimum horizontal stress $S_{h\ min}$	33.78 MPa (4900 psi)
Maximum horizontal stress $S_{h\ max}$	34.47 MPa (5000 psi)
Vertical stress S_v	48.26 MPa (7000 psi)
Ambient pore pressure p_0	26.89 MPa (3900 psi)
Net fracturing pressure p_{net}	3.45 MPa (500 psi)
Inherent cohesion strength of the intact rock S_0	20 MPa (2900 psi)
Inherent cohesion strength of weak zones S_{0w}	2 MPa (290 psi)
Treatment depth	2.29 km (7500 ft)
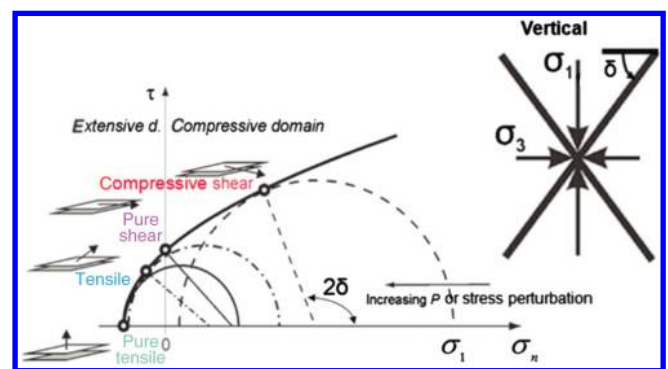
Figure 9. Schematic illustration of the generation of four different failure types using the Mohr Circle and Griffith failure envelope. According to the relations between shear stress τ and normal stress σ_n, the pure tensile, hybrid tensile ("tensile" hereafter), pure shear, and compressive shear failure modes are defined (modified after Fischer and Guest, 2011). The upper right panel shows the in situ principal stress directions relative to the fracture plane. For the case of waterfrac treatment in the Barnett Shale, the maximum principal stress is vertical. Therefore, the fracture dip determines the stress state at the failure point.
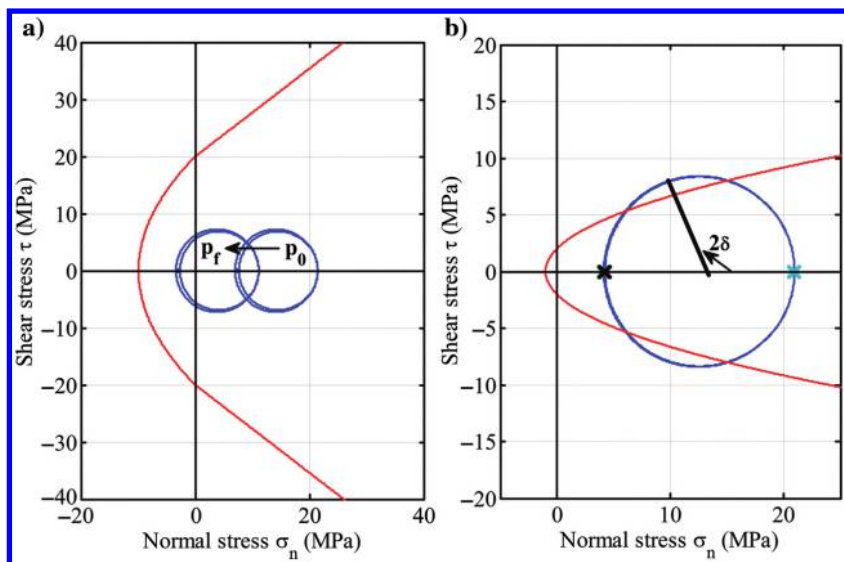
Figure 10. (a) The 3D Mohr circle representation of the stress state in the Barnett Shale for a typical waterfrac treatment (treatment parameters are listed in Table 5). Here, only the pore pressure effect is considered. The blue circle on the right corresponds to the case of the ambient pore pressure p_0, whereas the left circle is associated with the maximum possible pore pressure case, where the pore pressure is increased to the fracturing pressure p_f. The Griffith failure envelope for the intact rock with the inherent cohesion strength S_0 of 20 MPa is shown as the red curve. (b) The 3D Mohr-circle representation of the tip region. The black, green, and cyan crosses denote the principal stresses along the original unperturbed Shmin (northwest–southeast), SHmax (northeast–southwest), and vertical directions, respectively. The hydrofracture induced stress perturbations are considered and no fracturing fluid leakage occurs in the tip region. The Griffith failure envelope for weak zones with the inherent cohesion strength S_{0w} of 2 MPa is plotted as the red curve.
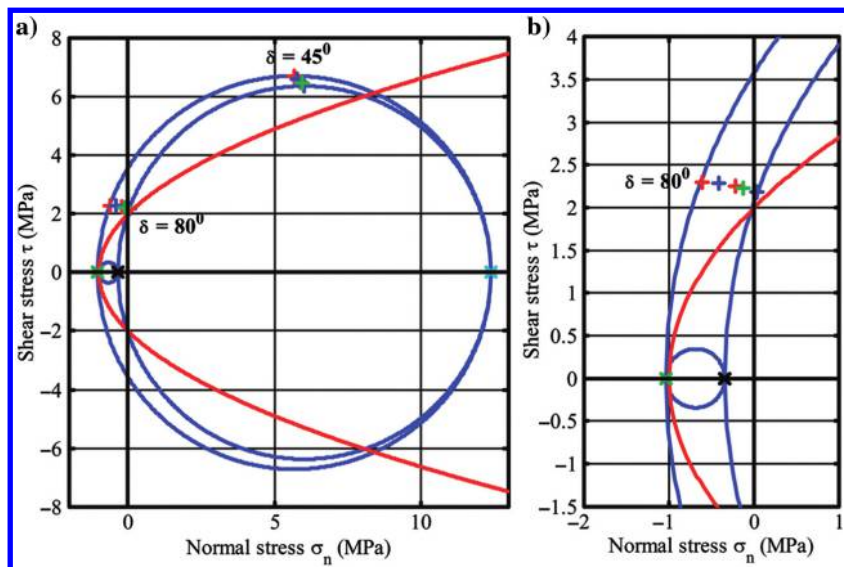

Figure 11. (a) The 3D Mohr-circle representation of the broadside region. In this figure, the hydrofracture-induced stress perturbations are considered. Fracturing fluid leakage is assumed in the broadside region to facilitate the generation of microseismicity. The red, green, and blue pluses demonstrate the normal and shear stresses on the fracture planes with strike angles of (80°, 140°), (10°, 70°), and (−15°, 45°), respectively (corresponding to west-northwest, northeast–southwest and north–south directions). The corresponding dip angles of these fracture planes are also listed. (b) Zoomed version of Figure 11a.

It is worth pointing out that the stress perturbation values chosen for the tip and broadside region in the analysis above are not meant to be an accurate representation of the in situ stress changes but to serve as the typical scoping parameters. Nevertheless, some general conclusions regarding microseismicity in the Barentt shale can still be drawn. First, microseismicity is very unlikely to occur in the intact rock because of its large cohesion strength. Therefore, weak zones like natural fractures are critical for hydraulic fracturing in the Barnett Shale (Gale et al., 2007; Gale and Holder, 2010). Second, rock failure could happen on the preferred weak zones in the tip region and the broadside region. The pore pressure increase due to fracturing fluid leakage is essential for microseismicity in the broadside region, whereas tensile stress perturbations incurred by the hydraulic fracture facilitate the generation of microearthquakes in the tip region. Possible weak zones in the Barnett Shale include natural fractures and the newly created hydraulic fractures. Two sets of dominant natural fractures were reported to be in the west-northwest and north–south directions, respectively (Gale et al., 2007; Gale and Holder, 2010). Finally, for reservoirs with a low horizontal differential stress and in normal faulting regimes, such as the Barnett Shale reservoir, rock failure could occur along almost any strike direction. The tensile events tend to occur at high dip angles, whereas compressive shear events are normally associated with low dip angles. This observation suggests that we could assign the high dipping plane as the fracture plane for tensile events and treat the low dipping plane as the fracture plane for compressive shear events. This justifies the synthetic sources we assumed in the previous synthetic study section. In the following field study section, we will use this approach to distinguish the fracture plane from the auxiliary plane. Moreover, it is worth mentioning that fracture strike instead of fracture dip will determine the failure types in the strike-slip faulting regime, where the maximum principal stress is horizontal.

MT inversion and source mechanism determination: Results and discussions

In this section, we apply the grid-search based full-waveform inversion approach to the 42 selected events to invert for the complete MT. The tensile earthquake source parameters including FPS (strike ϕ, dip δ, rake λ), the slope angle α, k, the V_P/V_S ratio at the focal area, seismic moment M_0, MT magnitude M_w, and DC, isotropic, and CLVD component percentages are also estimated from the inverted MTs. We will begin with one field event, named G1-1, to demonstrate the

procedure of the complete MT inversion and source parameter estimation using full waveforms. After that, we will present the source mechanism results for all 42 chosen events and discuss their implications in understanding the fracturing process and the reservoir.

Figure 12 demonstrates the process of the grid-search based MT inversion of the field event G1-1 using the layered model illustrated in Table 1 and Figure 2a. On Figure 12a, the normalized variance reduction is plotted as a function of searched event location and origin time. The black star denotes the initial source location and origin time estimate, and the white star gives the inverted source location and origin time. It is clear that the variance reduction function VAR is maximized at the inverted source location and origin time, suggesting a better waveform fit than the initial event location and origin time. Figure 12b presents the VAR at the inverted source location as a function of origin time. It is observed that the VAR is periodical with respect to the time shift. A comparison between Figure 12a and 12b indicates that the periodicity of VAR with respect to the time shift is more pronounced than that to the source location. This is caused by inverting seismograms of a limited frequency band between 100 and 300 Hz. A wider frequency band gives a better resolution but a less stable inversion result. This is because a larger frequency bandwidth requires a more accurate velocity model and an energetic signal across a wide frequency band, which is difficult to achieve in the field. Therefore, the selection of the filtering bandwidth of [100, 300] Hz is to balance the tradeoff between the inversion stability and the solution resolution. Moreover, the selected frequency band should also cover the event corner frequencies to avoid the saturation effect (Viegas et al., 2012).

Figure 13 shows the best waveform fitting for the field event G1-1. A good agreement in dominant P- and S-wave trains between modeled data in black and observed data in red is seen on both components. It is worth pointing out that the noisy feature on the modeled data of well 2 in Figure 13a is not due to numeric noise but as a result of the large scaling factor of 11.65 used in the plot. The actual waveform amplitude of the north component from well 2 is much smaller than that from well 1. In this example event, we did not notice significant unmodeled wave packages. In some other events, we observed some degree of unmodeled wave packages between P- and S-arrivals, which probably points to the presence of a complex laterally inhomogeneous structure in this area. Overall, a good agreement in dominant P- and S-wave packages between modeled data and observed data is observed for all 42 events.

From the inverted MT of this field event G1-1, two planes with strike, dip, and rake of (16°, 79°, 70°), (343°, 32°, 229°) are derived. The slope α is estimated to be 37°. Even considering the possible error of 14° in the slope angle due to data noise, source mislocations and velocity model errors as discussed in the synthetic study, the field event G1-1 is considered to be tensile. Moreover, as illustrated in the synthetic study, the dip angle is the most reliably determined parameter (see the analysis in Table 4). Therefore, the plane with the larger dip angle of 79° is selected as the fracture plane following the conclusion drawn from geomechanical analysis. The fracture strike is estimated to be 16°. As illustrated in the synthetic study, the strike angle ϕ is the least accurate source parameter estimate with an error up to 22° for event group G1 (see Table 4). The fracture strike associated with field event G1-1 is considered to be consistent with the north–south direction. Therefore, event G1-1 is attributed to the tensile opening of the north–south natural fracture.

Furthermore, the F test has been performed to test the significance of non-DC components by taking into account the variance reductions in the MT and pure DC inversions, and the corresponding numbers of degrees of freedom in the observed data (Šílený et al., 2009). It turns out for event G1-1, at a confidence level of 99.9%, the MT model is better than the DC source model in satisfying the observed data. Actually, for all the 42 events under investigation, at a confidence level higher than 95%, the MT model is preferred to describe the observed data. In other words, the probability of the existence of the non-DC source is significant.

The same procedure is then applied to all the selected events (see Table 6). It is observed that all the events except the six underlined events are adequately fit by the tensile earthquake model. The six underlined events have k-values beyond the physical limit described in equations 9 and, therefore, cannot be modeled by the tensile
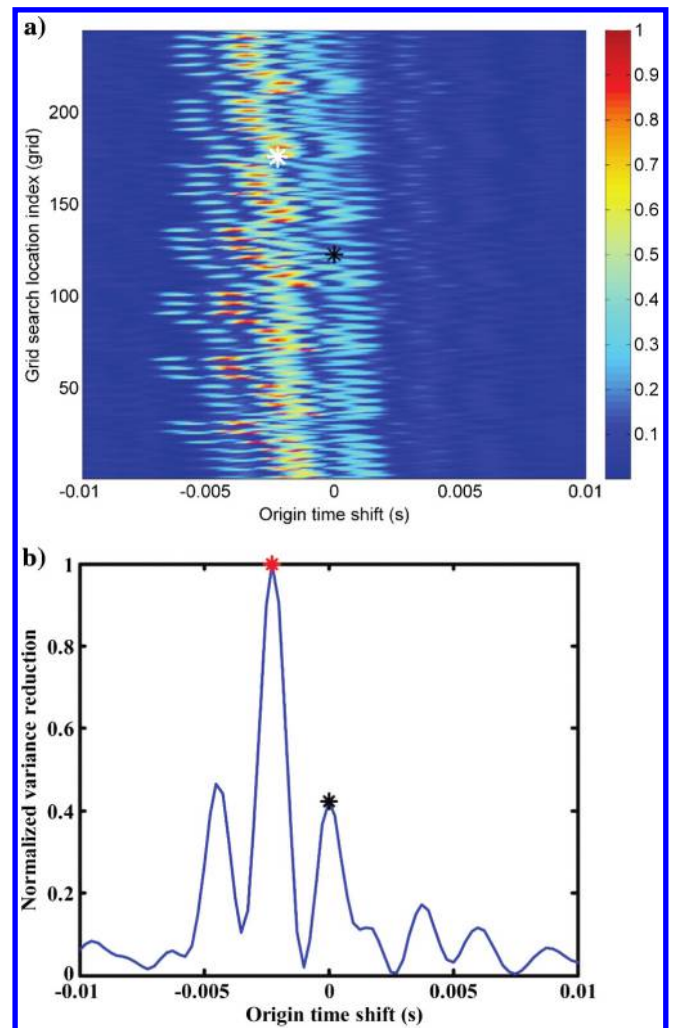

Figure 12. MT inversion for the field event G1-1. (a) The normalized variance reduction as a function of searched event origin time and event location. The initial event location and origin time is shown as the black star, and the grid search inverted event location and origin time is plotted as the white star. (b) The normalized variance reduction as a function of searched event origin time at the optimum event location. The initial and inverted event origin times are plotted as the black and red stars, respectively.

earthquake model of Vavryčuk (2001). The reason for this behavior is not clear. It may be due to the higher complexity in these six events that cannot be modeled by the simple tensile earthquake model. Nevertheless, we will focus our attention on the remaining 36 events in the following discussion.

Figure 14 gives the beachball plot of the inverted source mechanisms for these 36 events. The red lines indicate the fracture plane, and the black lines represent the auxiliary plane. Considering the possible error in the strike estimate as described in the synthetic study (see Table 4), the 36 events can be moved into three groups with different fracture orientations: 11 events striking in the northeast–southwest direction are shown as black in Table 6 ("black events" hereafter), three events striking along the west-northwest direction are depicted in blue ("blue events" hereafter), and the remaining 22 events striking approximately along the north–south direction are listed in red ("red events" hereafter). As mentioned previously, Gale et al. (2007) identify two sets of dominant natural fractures along the west-northwest and north–south directions, respectively. Pre- and postinjection borehole image logs and cored intervals suggest that, in structurally complex areas, multiple hydraulic fracture strands are likely to propagate along the SHmax direction (Warpinski et al., 1993; Fast et al., 1994). Geologic discontinuities, such as joints, faults, and bedding planes, have been found to contribute to the creation of multiple hydraulic fracture strands mapped during mineback experiments and generated in laboratory tests (Warpinski and Teufel, 1987). Recently, numerical studies also indicate that the interaction between preexisting natural fractures and the advancing hydraulic fracture is a key condition leading to complex hydraulic fracture patterns (Dahi-Taleghani and Olson, 2011). Therefore, it is likely that multiple hydraulic fractures oriented subparallel to the SHmax direction, i.e., the northeast–southwest direction, would form because of the interaction of the main advancing hydraulic fracture and preexisting natural fractures in the Barnett Shale. Hence, we may attribute the identified three groups of events in black, blue, and red to rock failures on the hydraulic fractures in the northeast–southwest direction, the west-northwest, and north–south oriented natural fractures, respectively.

It is observed in Table 6 that all 11 black events striking along the northeast–southwest direction have positive slope angles. Even if the possible errors in the slope estimate are considered, at least nine black events have nonnegligible positive slope angles, despite the fact that the other two black events have slope angles close to 0°. We interpret that these events striking along the northeast–southwest direction may indicate the tensile opening of multiple hydraulic fractures trending subparallel to the SHmax direction.

The fracture plane orientation of the blue and red events is close to the natural fracture orientation. We speculate that these events correspond to the reactivation of west-northwest and north–south oriented natural fractures. Most of these events have positive slope angles, in spite of the possible errors in the slope estimate as described in Table 4. This seems to indicate the existence of tensile opening associated with the reactivation of natural fractures. Nevertheless, nonnegligible negative slope angles are also seen for some blue and red events, such as events G1-3, G1-11, G1-14, G1-18, G3-1, and G3-3. One question arises, that is, how could these compressive shear events on natural fractures improve the permeability and enhance gas production? One possible explanation would be the fracture roughness. The shearing process causes the calcite filling inside the natural fractures to break, which creates open spaces. The compressive stress may decrease the volume of some void spaces, but the asperities could help preserve some of the newly created flow paths and, therefore, support an increase in permeability.

The moment magnitude for all the events is found to range from zero to −3, with the majority falling into the range of −1 to −3, even after taking into account a possible error in seismic moment estimate up to 30%.

It is observed in Table 6 that the V_P/V_S ratio in the focal area is generally lower than that of the surrounding medium where seismic waves propagate. This behavior was also reported in the seismological study of tensile faulting by Fojtíková et al. (2010). It is also interesting to see that some of the largest derived V_P/V_S ratios ($V_P/V_S > 1.7$ for events G4-8, G1-17, G2-2) appear in the events occurring on the hydraulic fractures trending subparallel to the SHmax direction. Even considering the possible uncertainty in the k-estimate resulting from data noise and velocity model inaccuracies, this observation still holds. These large V_P/V_S ratios, close to that of the surrounding medium, might be a sign of the newly formed hydraulic fractures instead of activation of preexisting natural fractures.

Furthermore, in terms of component percentages, many events from the group G1, G4 seem to have CLVD as the dominant

Figure 13. Waveform fitting for field event G1-1. Modeled seismograms derived from grid-search based complete MT inversion are shown in black, and the observed seismograms are plotted in red. (a) North component. (b) East component. The relative scaling factors between well 1 (geophones 1–12) and well 2 (geophones 13–24) are listed. The inversion is performed on the band-pass filtered horizontal components and uses the layered model shown in Figure 2a) and Table 1.
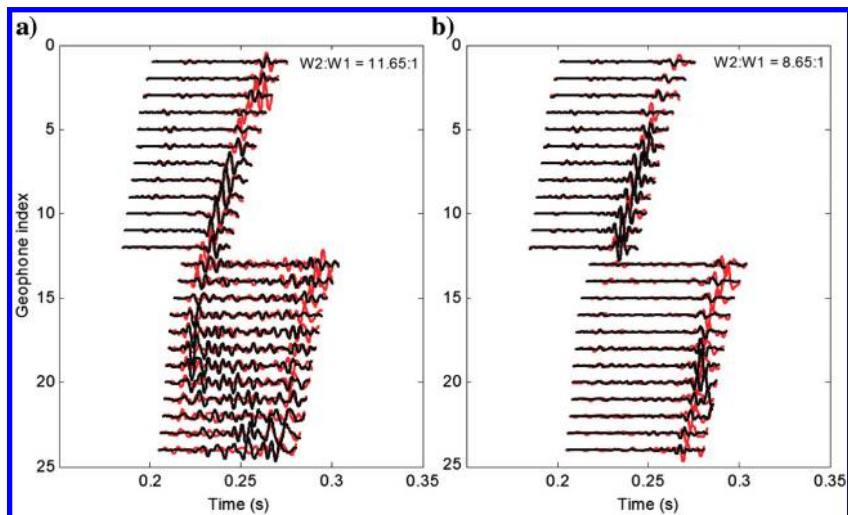
component. Two possible reasons for this behavior are (1) errors in CLVD component and (2) the mechanism associated with hydraulic fracturing in these complex fractured gas shales.

The possibility of a large error in CLVD component percentage for event groups G1 and G4 is very real because of their larger condition numbers, as seen from Table 4. According to Hardebeck and Shearer (2003), pure DC events tend to have a small P/S amplitude ratio averaged around 0.1. Good quality events for location and MT inversion generally require a strong P-wave. Therefore, there might be a possibility of event selection bias.

Alternatively, for some events in the groups G1 and G4, the analysis might be correct and a large CLVD component may be

Table 6. Results of source mechanism determinations for the 42 selected microseismic events.

Event ID	M_0 (10^7 N·m)	M_w	k	$\frac{V_P}{V_S}$	α (°)	ϕ (°)	δ (°)	λ (°)	DC (%)	ISO (%)	CLVD (%)	Cond. Num.
G1-1	0.92	−1.4	0.10	1.45	37	16	79	70	24	28	48	6
G1-2	3.30	−1.1	0.02	1.42	40	20	86	51	22	26	52	9
G1-3	1.00	−1.4	0.17	1.47	−31	4	28	81	30	−27	−43	14
G1-4	1.30	−1.3	0.46	1.57	39	170	87	240	20	37	43	17
G1-5	0.24	−1.8	−0.02	1.40	41	206	88	336	21	26	53	30
G1-6	0.62	−1.5	0.00	1.41	45	16	87	63	17	28	55	12
G1-7	1.87	−1.2	0.02	1.42	51	11	89	79	13	29	58	21
G1-8	0.47	−1.6	−0.03	1.40	57	349	80	145	9	30	61	11
G1-9	1.04	−1.4	−0.04	1.40	44	15	80	65	19	26	55	17
G1-10	2.49	−1.1	0.00	1.41	64	16	78	26	5	32	63	17
G1-11	0.27	−1.8	−0.01	1.41	−46	347	55	26	17	−27	−56	19
G1-12	0.17	−1.9	0.15	1.46	−14	326	65	358	59	−16	−25	10
G1-13	0.16	−1.9	0.06	1.44	53	25	74	7	11	31	58	22
G1-14	0.07	−2.2	−0.20	1.34	−33	338	67	358	31	−18	−51	6
G1-15	0.27	−1.8	−0.02	1.41	38	37	77	26	24	25	51	12
G1-16	0.16	−1.9	−0.01	1.41	16	50	77	24	58	14	28	12
G1-17	0.33	−1.7	1.12	1.77	2	59	89	34	93	4	3	14
G1-18	0.12	−2.0	−0.01	1.41	−23	347	52	17	44	−19	−37	15
G2-1			−3.40									
G2-2	0.17	−1.9	0.97	1.72	12	31	87	293	56	24	20	11
G2-3	0.62	−1.5	−0.02	1.41	47	199	83	74	16	27	57	9
G2-4			−1.87									
G2-5	0.09	−2.0	0.00	1.42	21	200	89	101	48	18	34	10
G2-6			−2.18									
G3-1	0.06	−2.2	−0.09	1.38	−21	125	42	156	49	−15	−36	4
G3-2	0.18	−1.9	0.34	1.53	21	64	82	152	43	25	32	8
G3-3	0.07	−2.2	0.28	1.51	−20	286	57	146	46	−22	−32	12
G3-4			−0.81									
G3-5			−1.05									
G3-6			−2.01									
G3-7	0.47	−1.6	0.26	1.50	36	49	88	193	24	45	31	10
G3-8	0.95	−1.4	−0.06	1.39	26	57	89	159	40	19	41	9
G3-9	0.23	−1.8	0.34	1.53	15	228	85	199	54	20	26	11
G3-10	0.92	−1.4	0.08	1.44	32	285	90	19	30	25	45	10
G4-1	1.43	−1.3	−0.05	1.40	−31	334	72	4	32	−22	−46	28
G4-2	0.97	−1.4	0.00	1.41	−57	349	75	7	9	−30	−61	23
G4-3	1.50	−1.3	0.00	1.41	−50	346	74	8	13	−29	−58	28
G4-4	1.08	−1.4	0.04	1.43	38	35	87	27	24	26	50	33
G4-5	0.83	−1.5	0.04	1.43	−40	344	73	5	22	−27	−51	27
G4-6	1.66	−1.3	0.11	1.45	41	208	88	322	20	29	51	33
G4-7	7.26	−0.8	−0.03	1.40	−49	344	71	13	14	−28	−58	34
G4-8	0.52	−1.6	1.37	1.84	2	230	84	156	89	7	4	42

Note 1: The strike, dip, rake, and slope angles follow the convention of Aki and Richards (2002), and are defined in Figure 1.

Note 2: The underlined events are classified as events that can not be modeled by the tensile earthquake model of Vavryčuk (2001). The highlighted events in red and blue are classified as events associated with reactivation of natural fractures striking along north-south and west-northwest directions, respectively. The rest of the events in black, except the underlined events, correspond to the events striking along SHmax (northeast-southwest) directions.

physical, reflecting the properties of the earthquake source or of the medium in the focal area. On one hand, this could be an indicator of the presence of tensile faulting, manifested by a positive correlation between the ISO and CLVD components (Vavryčuk, 2001). On the other hand, the large CLVD component can arise from near-simultaneous faulting on fractures of different orientations or on a curved fracture surface (Nettles and Ekström, 1998).

Finally, it is worth drawing a comparison of the microseismic source mechanisms between the Barnett Shale case and the Bonner tight gas sands case (Song and Toksöz, 2011). The microseismic map in the Bonner tight gas sands delineates a simple planar geometry. Although only one-well data set is available for the Bonner tight gas sands case, Song and Toksöz (2011) are able to use the constrained inversion to invert the source mechanisms for some events by matching full waveforms. The determined microseismic FPS in the Bonner sands also suggests a dominant fracture plane orientation close to the average fracture trend derived from multiple event locations. The retrieved source mechanisms indicate a predominant DC component. This seems to suggest that in a simple reservoir with a high horizontal differential stress (around 3 MPa), such as the Bonner sands, the microseismicity occurs as predominantly shearing along natural fractures subparallel to the average fracture trend. Increased production is obtained in reservoirs like Bonner gas sands through the improved fracture conductivity. On the contrary, in a fractured reservoir with a low horizontal differential stress (around 0.7 MPa), such as the Barnett Shale,

the microseismic source mechanism study indicates that tensile and compressive shear events could occur on preferred weak zones such as preexisting natural fractures and newly created hydraulic fracture strands. In the normal faulting regime, where the maximum principal stress is vertical, tensile events tend to have higher dips. A complex fracture network is formed together with complex non-DC events. An enhanced production is achieved in reservoirs like the Barnett Shale through the increased fracture connectivity.

To summarize, weak zones such as newly created hydraulic fracture strands and calcite filled natural fractures inside the Barnett Shale play a critical role, not only in the production enhancement but also in the generation of microearthquakes during the hydrofracture treatment. The determined microseismic source mechanisms provide a wealth of information about the fracturing process and the reservoir. Results from geomechanical analysis indicate that all the microearthquakes occur on the weak zones surrounding the hydraulic fracture. Microearthquakes happen as the response of the reservoir to the hydrofracture perturbation. Therefore, in addition to hydraulic fracture mapping, microseismic monitoring could serve as a reservoir characterization tool.

CONCLUSIONS

In this paper, we have presented a comprehensive microseismic source mechanism study in the Barnett Shale in the Fort Worth Basin. We have used a grid-search based full-waveform inversion

Figure 14. The beachball representation of the inverted source mechanisms summarized in Table 6. Red lines on the beachball indicate the fracture plane, and black lines represent the auxiliary plane. Three groups of events with different fracture orientations are seen. The upper left and lower left plots correspond to the activation of preexisting natural fractures along the north–south and west-northwest directions, respectively (see the highlighted events in red and blue in Table 6). The right plot is associated with tensile failure on the hydraulic fractures trending subparallel to the northeast–southwest direction (see the events in black in Table 6).
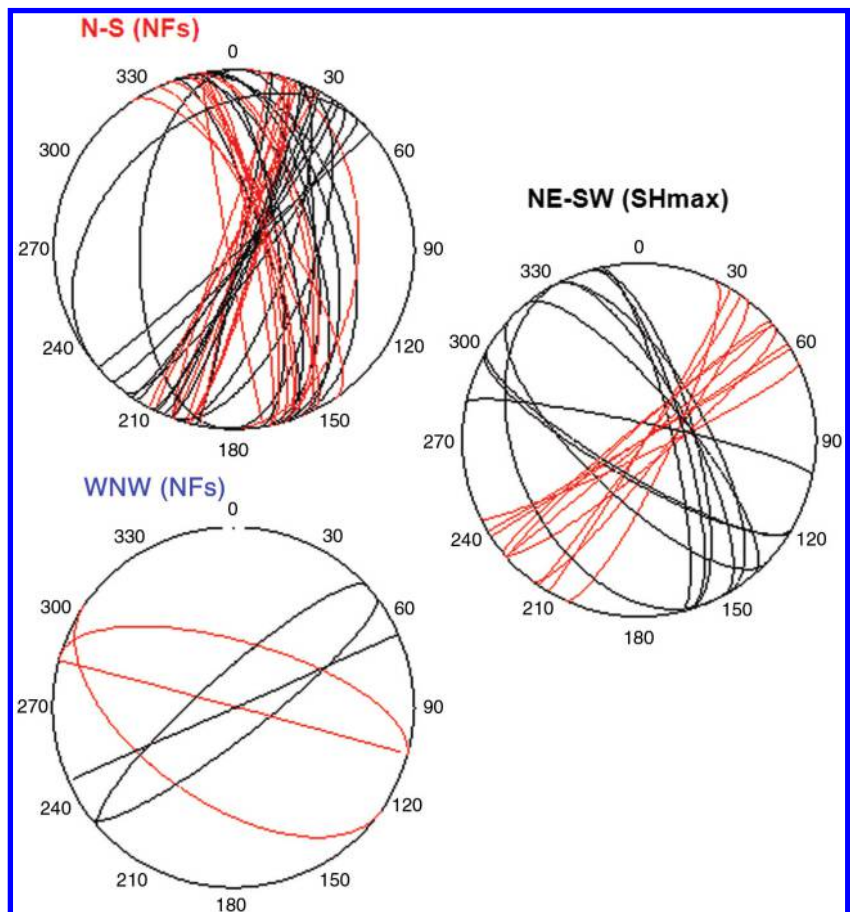
approach to determine the complete MT from a dual-array data set. We have estimated the source parameters for each event according to the tensile earthquake model. Both shear and tensile failures are accommodated in this model. The derived source parameters include the fault plane orientation, the slope angle, the V_P/V_S ratio in the focal area, and the seismic moment.

We have analyzed the microseismicity in the Barnett Shale using hydraulic fracture geomechanics. We have considered the pore pressure increase due to fracturing fluid leakage and the stress perturbations resulting from the hydraulic fracture in our analysis. We have used the Griffith criterion and the 3D Mohr circle to determine the failure types. Results indicate that weak zones are critical to the generation of microseismicity in the Barnett Shale. We find that tensile and compressive shear events could occur on preferred weak zones including natural fractures and hydraulic fractures. In the normal faulting regime, such as that encountered in the Barnett Shale, tensile events tend to have higher dips. We propose a method to distinguish the fracture plane from the auxiliary plane. The fracture plane is selected as the high-dipping plane for events with positive slope angles, and the low-dipping plane for events with negative slope angles.

In the synthetic study, we investigate the influence of velocity model errors, event mislocations, and additive data noise on the extracted source parameters via a Monte-Carlo test. We demonstrate that with a correct velocity model, the errors in the inverted source parameters are minimal, compared to the case of inversion with an inaccurate velocity model. We also show that a reasonable amount of error in source location and the velocity model, together with data noise, do not cause a serious distortion in the inverted MTs and source parameters. In our synthetic test, the fracture dip is proven to be the most reliable source parameter estimate with respect to velocity model errors, while the fracture strike has the largest inversion error resulting from velocity model inaccuracies. The synthetic test also indicates that with the same amount of velocity model errors and data noise, large source parameter errors occur when the condition number of the sensitivity matrix is high.

We have determined the source mechanisms for 42 good S/N and low condition number microseismic events induced by waterfrac treatment in the Barnett Shale. Results show that most events follow the tensile earthquake model and possess significant non-DC components. We have demonstrated the significance of the occurrence of non-DC components in these events by F-test. The inverted source mechanisms reveal tensile opening on the hydraulic fracture strands trending subparallel to the unperturbed SHmax direction and the reactivation of preexisting natural fractures along west-northwest and north–south directions. An increased fracture connectivity and enhanced gas production in the Barnett Shale are achieved through the formation of a complex fracture network during hydraulic fracturing via rock failures on the weak zones of various orientations.

Potential errors in source parameter estimates from dual-array data primarily come from the unmodeled velocity and attenuation model errors. An extended study of the influence of attenuation and anisotropy will be carried out in the future. Full-waveform based microseismic source mechanism study not only reveals important information about the fracturing mechanism, but also allows fracture characterization away from the wellbore, providing critical constraints for understanding fractured reservoirs.

REFERENCES

Agarwal, K., M. J. Mayerhofer, and N. R. Warpinski, 2012, Impact of geomechanics on microseismicity: SPE 152835.

Aki, K., and P. G. Richards, 2002, Quantitative seismology: University Science Books.

Baig, A., and T. Urbancic, 2010, Microseismic moment tensors: A path to understanding frac growth: The Leading Edge, **29**, 320–324, doi: 10.1190/1.3353729.

Birkelo, B., K. Cieslik, B. Witten, S. Montgomery, B. Artman, D. Miller, and M. Norton, 2012, High-quality surface microseismic data illuminates fracture treatments: A case study in the Montney: The Leading Edge, **31**, 1318–1325, doi: 10.1190/tle31111318.1.

Bouchon, M., 2003, A review of the discrete wavenumber method: Pure and Applied Geophysics, **160**, 445–465, doi: 10.1007/PL00012545.

Bruner, K., and R. Smosna, 2011, A comparative study of the Mississippian Barnett Shale, Fort Worth Basin, and Devonian Marcellus Shale, Appalachian Basin: U. S. Department of Energy/National Energy Technology Laboratory publication DOE/NETL-2011/1478.

Busetti, S., K. Mish, P. Hennings, and Z. Reches, 2012, Damage and plastic deformation of reservoir rocks: Part 2: Propagation of a hydraulic fracture: AAPG Bulletin, **96**, 1711–1732, doi: 10.1306/02011211011.

Dahi-Taleghani, A., and J. E. Olson, 2011, Numerical modeling of multistranded-hydraulic-fracture propagation: Accounting for the interaction between induced and natural fractures: SPE Journal, **16**, 575–581, doi: 10.2118/124884-PA.

Eaton, D., and F. Forouhideh, 2011, Solid angles and the impact of receiver-array geometry on microseismic moment tensor inversion: Geophysics, **76**, no. 6, WC77–WC85, doi: 10.1190/geo2011-0077.1.

Eisner, L., B. J. Hulsey, P. Duncan, D. Jurick, H. Werner, and W. Keller, 2010, Comparison of surface and borehole locations of induced seismicity: Geophysical Prospecting, **58**, 809–820, doi: 10.1111/j.1365-2478.2010.00867.x.

Fast, R. E., A. S. Murer, and R. S. Timmer, 1994, Description and analysis of cored hydraulic fractures, Lost Hills field, Kern County, California: SPE production and facilities, **9**, 107–114, doi: 10.2118/24853-PA.

Fischer, T., and A. Guest, 2011, Shear and tensile earthquakes caused by fluid injection: Geophysical Research Letters, **38**, L05307.

Fisher, M. K., J. R. Heinze, C. D. Harris, B. M. Davidson, C. A. Wright, and K. P. Dunn, 2004, Optimizing horizontal completion techniques in the Barnett Shale using microseismic fracture mapping: SPE 90051.

Fojtíková, L., V. Vavryčuk, A. Cipicar, and J. Madarás, 2010, Focal mechanisms of micro-earthquakes in the Dobrá Voda seismoactive area in the Malé Karpaty Mts. (Little Carpathians), Slovakia: Tectonophysics, **492**, 213–229, doi: 10.1016/j.tecto.2010.06.007.

Gale, J. F. W., and J. Holder, 2008, Natural fractures in the Barnett Shale: Constraints on spatial organization and tensile strength with implications for hydraulic fracture treatment in shale-gas reservoirs: Proceedings of the 42nd US Rock Mechanics Symposium, Paper no. ARMA, 08-096.

Gale, J. F. W., and J. Holder, 2010, Natural fractures in some US shales and their importance for gas production: Petroleum Geology Conference Series 2010, Geological Society of London, **7**, 1131–1140.

Gale, J. F. W., R. M. Reed, and J. Holder, 2007, Natural fractures in Barnett Shale and their importance for hydraulic fractures treatments: AAPG Bulletin, **91**, 603–622, doi: 10.1306/11010606061.

Green, A. E., and I. N. Sneddon, 1950, The distribution of stress in the neighbourhood of a flat elliptic crack in an elastic solid: Mathematical Proceedings of the Cambridge Philosophical Society, **46**, 159–163.

Hardebeck, J. L., and P. M. Shearer, 2003, Using S/P amplitude ratios to constrain the focal mechanisms of small earthquakes: Bulletin of the Seismological Society of America, **93**, 2434–2444, doi: 10.1785/0120020236.

Herrmann, R. B., 1975, A student's guide to the use of P and S wave data for focal mechanism determination: Earthquake Notes, **46**, 29–39.

Johnston, D., 2004, Technological advances expand potential play: Oil and Gas Journal, **102**, no. 3, 51–59.

Kawakatsu, H., and J. Montagner, 2008, Time-reversal seismic-source imaging and moment-tensor inversion: Geophysical Journal International, **175**, 686–688, doi: 10.1111/j.1365-246X.2008.03926.x.

Lancaster, D. E., S. McKetta, and P. H. Lowry, 1993, Research findings help characterize Fort Worth Basin's Barnett Shale: Oil and Gas Journal, **91**, no. 10, 59–64.

Li, J., H. S. Kuleli, H. Zhang, and M. N. Toksöz, 2011, Focal mechanism determination of induced microearthquakes in an oil field using full waveforms from shallow and deep seismic networks: Geophysics, **76**, no. 6, WC87–WC101, doi: 10.1190/geo2011-0030.1.

Maxwell, S. C., J. Rutledge, R. Jones, and M. Fehler, 2010, Petroleum reservoir characterization using downhole microseismic monitoring: Geophysics, **75**, no. 5, 75A129–75A137, doi: 10.1190/1.3477966.

Nettles, M., and G. Ekström, 1998, Faulting mechanism of anomalous earthquakes near Bardarbunga Volcano, Iceland: Journal of Geophysical Research, **103**, 17973–17984, doi: 10.1029/98JB01392.

Ramsey, J. M., and F. M. Chester, 2004, Hybrid fracture and the transition from extension fracture to shear fracture: Nature, **428**, 63–66, doi: 10.1038/nature02333.

Roth, M., and A. Thompson, 2009, Fracture interpretation in the Barnett Shale using macro- and microseismic data: First Break, **27**, 83–88.

Rutledge, J. T., W. S. Phillips, and M. J. Mayerhofer, 2004, Faulting induced by forced fluid injection and fluid flow forced by faulting: An interpretation of hydraulic-fracture microseismicity, Carthage Cotton Valley gas field, Texas: Bulletin of the Seismological Society of America, **94**, 1817–1830, doi: 10.1785/012003257.

Shemeta, J. E., S. Maxwell, N. R. Warpinski, S. Quimby, T. Riebel, Z. Phillips, J. R. Kinser, G. Hinds, T. W. Green, and C. K. Waltman, 2007, Stacking seismograms to improve passive microseismic images: SPE 108103.

Šílený, J., D. P. Hill, L. Eisner, and F. H. Cornet, 2009, Non-double-couple mechanisms of microearthquakes induced by hydraulic fracturing: Journal of Geophysical Research, **114**, B08307, doi: 10.1029/2008JB005987.

Song, F., and M. N. Toksöz, 2011, Full-waveform based complete moment tensor inversion and source parameter estimation from downhole microseismic data for hydrofracture monitoring: Geophysics, **76**, no. 6, WC103–WC116, doi: 10.1190/geo2011-0027.1.

Thomsen, L., 1986, Weak elastic anisotropy: Geophysics, **51**, 1954–1966, doi: 10.1190/1.1442051.

Toksöz, M. N., and D. H. Johnston, 1981, Seismic wave attenuation: SEG.

Tran, D. T., J. Roegiers, and M. Thiercelin, 2010, Thermally-induced tensile fractures in the Barnett Shale and their implications to gas shale fracability: Proceedings of the 44th US Rock Mechanics Symposium, Paper no. ARMA 10-466.

Vavryčuk, V., 2001, Inversion for parameters of tensile earthquakes: Journal of Geophysical Research, **106**, 16339–16355, doi: 10.1029/2001JB000372.

Vavryčuk, V., 2007, On the retrieval of moment tensors from borehole data: Geophysical Prospecting, **55**, 381–391, doi: 10.1111/j.1365-2478.2007.00624.x.

Vavryčuk, V., 2011, Tensile earthquakes: Theory, modeling, and inversion: Journal of Geophysical Research, **116**, B12320, doi: 10.1029/2011JB008770.

Viegas, G., A. Baig, W. Coulter, and T. Urbancic, 2012, Effective monitoring of reservoir-induced seismicity utilizing integrated surface and downhole seismic networks: First Break, **30**, 77–81.

Warpinski, N. R., 1991, Hydraulic fracturing in tight, fissured media: Journal of Petroleum Technology, **43**, 146–151, 208–209, doi: 10.2118/20154-PA.

Warpinski, N. R., and J. Du, 2010, Source-mechanism studies on microseismicity induced by hydraulic fracturing: SPE 135254.

Warpinski, N. R., R. C. Kramm, J. R. Heinze, and C. K. Waltman, 2005, Comparison of single- and dual-array microseismic mapping techniques in the Barnett Shale: SPE 95568.

Warpinski, N. R., J. C. Lorenz, P. T. Branagan, F. R. Myal, and B. L. Gall, 1993, Examination of a cored hydrofracture in a deep gas well: SPE production and facilities, **8**, no. 3, p. 150–158, doi: 10.2118/22876-PA.

Warpinski, N. R., M. J. Mayerhofer, K. Agarwal, and J. Du, 2012, Hydraulic fracture geomechanics and microseismic source mechanisms: SPE 158935.

Warpinski, N. R., and L. W. Teufel, 1987, Influence of geologic discontinuities on hydraulic fracture propagation: Journal of Petroleum Technology, **39**, 209–220, doi: 10.2118/13224-PA.

Warpinski, N. R., C. K. Waltman, J. Du, and Q. Ma, 2009, Anisotropy effects in microseismic monitoring: SPE 124208.

Zoback, M., 2007, Reservoir geomechanics: Cambridge University Press.

This article has been cited by:

1. Vladimir GrechkaMoment tensor inversion of single-well microseismic data: Is it feasible? 2506-2511. [Abstract] [References] [PDF] [PDF w/Links]
2. Vladimir Grechka. 2015. On the feasibility of inversion of single-well microseismic data for full moment tensor. *GEOPHYSICS* **80**:4, KS41-KS49. [Abstract] [Full Text] [PDF] [PDF w/Links]
3. Rob Westaway, Paul L. Younger, Chris Cornelius. 2015. Comment on 'Life cycle environmental impacts of UK shale gas' by L. Stamford and A. Azapagic. Applied Energy, 134, 506–518, 2014. *Applied Energy* **148**, 489-495. [CrossRef]